

Evolutionary Multi-Objective Optimization of Color Pixels based on Dielectric Nano-Antennas

Peter R. Wiecha,^{1,*} Arnaud Arbouet,^{1,†} Christian Girard,¹
Guilhem Larrieu,² Aurélie Lecestre,² and Vincent Paillard^{1,‡}

¹*CEMES-CNRS, Université de Toulouse, CNRS, UPS, Toulouse, France*

²*LAAS-CNRS, Université de Toulouse, CNRS, INP, Toulouse, France*

The rational design of photonic nanostructures consists in anticipating their optical response from simple models or as variations of reference systems. This strategy is limited when different objectives are simultaneously targeted. Inspired from biology, evolutionary approaches drive the morphology of a nano-object towards an optimum through several cycles of selection, mutation and cross-over, mimicking the process of natural selection. However, their extension to scenarii with multiple objectives demands efficient computational schemes. We present a numerical technique to design photonic nanostructures with optical properties optimized along several arbitrary objectives. This combination of evolutionary multi-objective algorithms with frequency-domain electro-dynamical simulations is used to design silicon nanostructures resonant at user-defined, polarization-dependent wavelengths. The spectra of pixels fabricated by electron beam lithography following the optimized design show excellent agreement with the targeted objectives. The method is self-adaptive to arbitrary constraints, and therefore particularly interesting for the design of complex structures within technological limits.

Over the last decade, the field of nanophotonics or nano-optics has been rapidly increasing, mainly driven by plasmonics since noble metal nanoparticles can enhance and confine electromagnetic fields on the nanometer scale. By adapting the particle shape and dimensions, it is possible to spectrally tune plasmon resonances and tailor several optical properties such as the scattering spectrum¹, directional scattering,² polarization conversion³, heat generation⁴ optical chirality⁵ or nonlinear light emission.⁶ Similarly to plasmonics, high-index dielectric nanostructures have gained increasing interest as their high refractive index can also lead to both strong electric and magnetic field enhancement.^{7,8} The ability to provide exceptionally strong magnetic field enhancement without requiring complex geometries is an example in which high-index dielectrics can outperform plasmonic nanoantennas.^{9,10}

Such resonances can be used for field-enhanced spectroscopy,¹¹ for transmissive metasurfaces,¹² to enhance nonlinear effects^{13,14} or to obtain directional scattering due to interferences between electric and magnetic modes.¹⁵ Another key advantage of dielectrics is very low losses and consequently far higher laser damage thresholds compared to plasmonic materials.^{7,11,16} At last, the resonances in dielectric nanoparticles are spectrally tunable from the UV to the near IR.^{17–19}

When designing photonic nanostructures, a particular geometry is usually selected from qualitative considerations and its properties are subsequently studied systematically. As it comes to applications, a more convenient approach is to define the requested optical properties and design a nanostructure that optimally exhibits

the desired features. For the latter approach, a structure model has to be developed, which, based on a certain set of parameters, can describe in a generic way a large variety of particle geometries. However, this leads to huge parameter spaces which usually cannot be explored systematically within reasonable time. Thus trial-and-error is not an efficient search strategy. More promising techniques are evolutionary optimization strategies which, by mimicking natural selection, are able to find fittest parameter sets to a complex non-analytical problem.²⁰

In the field of nanophotonics, evolutionary algorithms have been applied to the maximization of field enhancement,^{21–24} scattering from plasmonic particles,^{25,26} or the design of hybrid plasmonic/dielectric antennas²⁷. Such methods were also successfully used on more technological applications like electron-beam field emission sources,²⁸ waveguide couplers²⁹ or core-shell nanoparticles for hyperthermia.³⁰

These studies were limited to the maximization of one target property at a specific wavelength and polarization. Such single-objective scenarii represent the simplest case of an optimization problem, while a structure that concurrently matches multiple objectives will be in general more difficult to design. In a recent work, genetic multi-objective optimization was used on plasmonic waveguides. A figure of merit describing the waveguide and its robustness against geometrical variations were maximized simultaneously.³¹ Evolutionary multi-objective optimization (EMO) strategies³² could lead to considerable improvements in the design of wavelength dependent (multi-)directional scattering,³³ multiresonant antennas³⁴ or polarization dependent tailored optical behavior³⁵. Nanoantennas possessing multiple resonances, for instance at the fundamental and harmonic frequencies,^{36,37} may also be optimized by EMO to enhance nonlinear effects.

In this paper, we present a combination of EMO with

* e-mail : peter.wiecha@cemes.fr

† e-mail : arnaud.arbouet@cemes.fr

‡ e-mail : vincent.paillard@cemes.fr

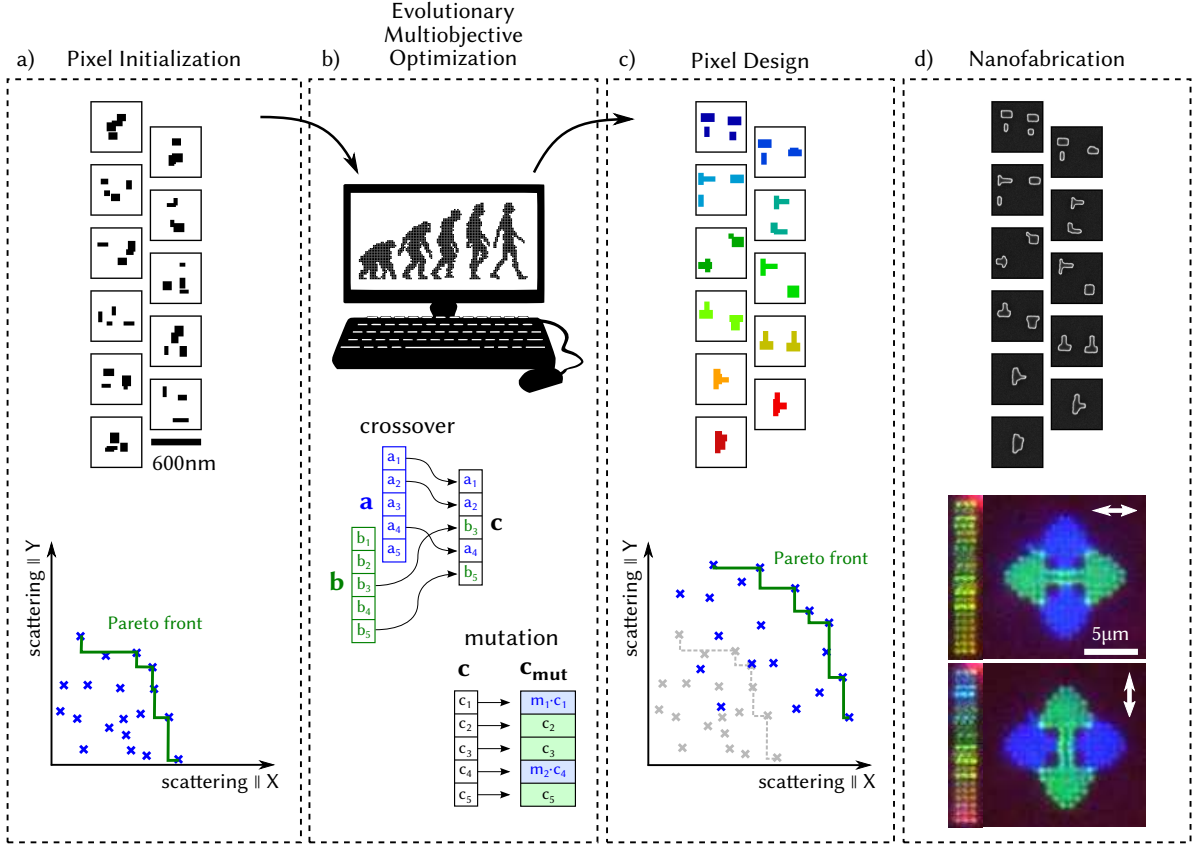


FIG. 1. **Illustration of evolutionary multi-objective optimization (EMO).** a) Initialization step of pixel-populations for the EMO algorithm. b) Evolution of the pixel-population. c) Optimum pixel-population at the end of the evolution. d) Nanofabrication and characterization of the polarization dependent color-pixels.

the Green Dyadic Method (GDM) for self-consistent full-field electro-dynamical simulations³⁸. We apply the EMO-GDM technique to design dielectric (silicon) nanoantennas that concurrently maximize the scattering at different wavelengths, dependent on the polarization of the incident light. With the computed EMO design, Si nanostructures are then fabricated on a SOI substrate and their optical response is measured by confocal dark-field scattering microscopy. These experiments show that the scattering properties are in excellent agreement with the optimization predictions.

I. OPTIMIZATION PROBLEM AND TECHNIQUE

A. Optimizing the Scattering Efficiency from Nanostructures

We illustrate the EMO-GDM technique with the scattering efficiency Q_{scat} as target property. Q_{scat} is defined as the ratio between the scattering cross-section σ_{scat} and the geometrical cross-section σ_{geom} (the “footprint”). Our goal is to maximize the scattering efficiency at a wave-

length λ_X , for an incident linear polarization along the X -axis, and simultaneously at a second wavelength λ_Y , for polarization along the Y -axis.

While this problem is mainly chosen for practical reasons – scattering and polarization are easily accessible values in the experiment – applications exist like holographic color-filters¹⁹ or color rendering and printing close to the diffraction limit. The latter has been demonstrated either using plasmonics^{1,39} or dielectric nanostructures¹⁷. Polarization dependent, dual-color pixels have been recently reported using plasmonic nanoapertures.⁴⁰ The advantage of plasmonic nanoantennas is the capability to provide widely tunable single mode responses using simple geometries (pillars in ref. 1, cuboids in ref. 39 and crosses in ref. 40). Dielectric nanostructures on the contrary often support high order and degenerate modes, occurring in a narrow spectral range. Therefore an EMO scheme is of particular interest for the design of multiresonant dielectric nanostructures.

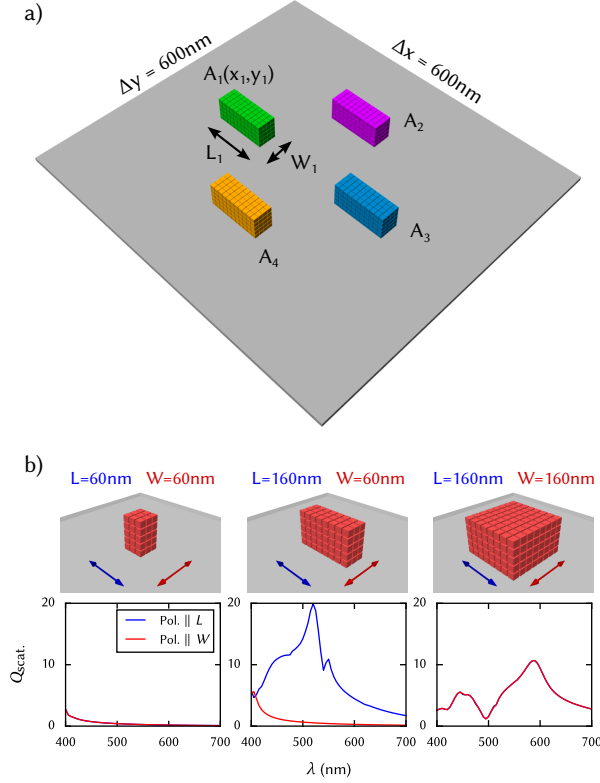


FIG. 2. **Structure model for EMO.** a) Example of silicon block arrangement forming a pixel. b) Scattering efficiencies calculated for individual silicon blocks of the minimum allowed size (left), minimum width and maximum length (center), and maximum possible size (right). The constraints are $L_{\min.} = W_{\min.} = 60 \text{ nm}$ and $L_{\max.} = W_{\max.} = 160 \text{ nm}$, the height is fixed to $H = 100 \text{ nm}$.

B. Evolutionary Multi-Objective Optimization

As illustrated in Figure 1, evolutionary optimization mimics the process of natural selection by defining a population of individuals, where each individual is in our case a set of parameters describing an antenna morphology. This population undergoes an evaluation and selection procedure in which weak solutions are eliminated and the fittest candidates (*i.e.* the parameter-sets yielding the best target values) are chosen to “mate” with each other. The target value of the optimization is also called the *fitness*. In our case, the target values are the scattering efficiencies at λ_X and λ_Y . The following process of reproduction usually consists of a step called *crossover*, where the parameters are exchanged and mixed – just like DNA in nature – and a *mutation* step, in which some randomly selected parameters are multiplied by or replaced with random numbers (see figure 1b). Like this, a new population of individuals is generated, the next generation. This process of selection, reproduction and evaluation is repeated until some stop-criterion is met, like a time limit or a maximum number of iterations.

In an optimization with a single objective, the initial

population is evolved until eventually the parameter-set that yields the best fitness is considered the optimum solution. In multi-objective problems however, the parameters describe not a single objective alone, but yield several target values that are all in parallel subject of the optimization. During the EMO evolution, this fitness-vector is therefore stored in an archive and remembered for comparison during the optimization. Once the evolution finished, the final solution is not trivially determined neither: A whole M -dimensional set of *non-dominated solutions* exists, with $M = (\text{Nr. of objectives} - 1)$. This final set of individuals is called the *Pareto-front*, which is the set of solutions that cannot be further optimized in one of the objectives, without worsening at least one other target value. There is no guarantee that the final solution converged to the absolute optimum but, due to the complexity of many problems, EMO is often the best possible approach.

C. Structure Model

The “population” of antenna morphologies to be considered in the computation must be diverse enough to explore, after several generations, a significant fraction of possible solutions. However, this requires a very large number of parameters, significantly slowing down convergence. Furthermore, the optimized geometries must remain within the limits of fabrication capabilities and have neither too many nor too small features. For these reasons we use a very simple model, based on four individual silicon elements with variable dimensions and positions, placed on a SiO_2 substrate ($n \approx 1.5$) within a limited area. A sketch of the model is shown in Fig. 2a.

Both, the x - and y -dimension of each antenna is allowed to vary between 60 nm and 160 nm, in steps of 20 nm, corresponding to the precision of a state-of-the-art electron-beam lithographic system. The height H is fixed to 100 nm, equal to the silicon overlayer thickness of our silicon-on-insulator (SOI) substrate. The antenna is placed within an area of $600 \times 600 \text{ nm}^2$. This constrained area ensures that the planewave excitation used in our simulations is a good approximation for the illumination loosely focused through a low-NA dark field objective.

For the electro-dynamical simulations, we use a volume integral technique in the frequency domain, namely the Green Dyadic method (GDM) which applies the concept of a generalized propagator (see [Methods](#))⁴¹. Exemplary spectra of single silicon-cuboids with dimensions corresponding to the size-limits used in our optimizations are shown in figure 2b. For simplicity, the positions are discretized in steps of 20 nm. In order to validate this large stepsize, we calculated spectra for the same structures using different discretization stepsizes, which yielded comparable results (see [supporting informations \(SI\), Sec. B](#)). Overlapping antennas are allowed, corresponding antennas are fused together accordingly.

The number of possible parameter combinations in this

model is larger than 1×10^{15} (see SI, Sec. A). We conclude that using the simple model described above, it is already inconceivable to use a brute-force strategy (evaluation of all possible combinations). We will therefore employ an EMO algorithm.

II. RESULTS AND DISCUSSION

A. Proof of Principle: $\lambda_X = \lambda_Y = 630$ nm

In a first step, we test the EMO-GDM technique on a simple problem. A single target wavelength $\lambda_{\text{max.}} = 630$ nm is selected, at which σ_{scat} is maximized simultaneously for X and Y polarization. The structures of the final population and the corresponding Pareto-front after an evolution over 200 generations are shown in Fig. 3a and 3b. The geometries of the initial population are compared to those on the Pareto-front in the [supporting informations, Sec. C](#).

The geometries found by evolutionary optimization are also transformed into a lithographic mask, which we use to produce the silicon nanostructures on a SOI substrate (see Methods). Fig. 3a shows a comparison of the design with SEM images of the sample. Simulated (Fig. 3c-d) and experimental spectra (Fig. 3e-f) are in very good agreement.

The outermost individuals on the Pareto-front (particles (1) and (40)) correspond to equivalent results of a single-objective optimization using one target wavelength and polarization. We observe in these cases, that all four sub-antennas are combined during the evolution to form a single rod-like antenna along the target polarization direction. In agreement with literature, this yields an optimum scattering efficiency with respect to the considered polarization direction (“1”: Y , “40”: X) – at the expense of a very low scattering for the respective perpendicular polarization.¹⁸ To obtain comparably high scattering efficiencies for both polarizations (particle “20” and neighbors), the evolution produces cross-like antennas.

B. Doubly Resonant Nanostructures by EMO-GDM

In a next step we study the maximization of Q_{scat} at two different wavelengths $\lambda_X = 550$ nm and $\lambda_Y = 450$ nm for mutually crossed polarizations. The randomly initialized population of 20 individuals at the beginning of the evolution (red), the Pareto-front (green) and selected structure designs as well as corresponding spectra are shown in figure 4. The individuals at the Pareto-front borders, labeled (1) and (3), correspond to single-objective optimizations for λ_Y and λ_X , respectively. Inspecting the three selected structures in more detail leads to the following observations.

Obviously twin structures like (1) and (2) seem to be preferred, because they result in an increase of the overall

scattering efficiency. Indeed, structures (1) and (2) both consist of two dimer antennas that, if taken individually, have about 30 %, respectively 10 %, lower Q_{scat} at the target wavelength of $\lambda_Y = 450$ nm compared to the twin structure. Furthermore, the peak positions in the scattering spectra are slightly shifted and match the target wavelengths only in the combined antenna.

We point out that the rather symmetric relative positioning of the two dimers is crucial for an optimum scattering efficiency. The configuration found by the evolutionary optimization is very close to the ideal positions. A marginally stronger scattering can be obtained for both structures (1) and (2), when the dimers are placed on the same horizontal axis but the possible gain is as low as about 3 % and 1 %, respectively.

At last, particle (3) in Fig. 4 consists only of a single dimer structure, which we attribute to the constrained maximum antenna size in our model. The maximization of the scattering at the longer target wavelength ($\lambda_X = 550$ nm) requires a larger amount of material compared to shorter wavelength λ_Y . The scattering efficiency can be further improved by allowing the algorithm to use larger or more constituents.

In the supporting informations, a detailed analysis of the structures (1) and (2) is shown ([section D, Figs. S4 and S5](#)), as well as a demonstration that the different geometry of structure (3) can be explained by the limited amount of silicon allowed in the computation ([section E](#)).

C. Tuning the Resonances of Silicon Nanoantennas

To further illustrate the EMO-GDM technique, we perform several multi-objective optimizations for different combinations of target wavelengths. The wavelength $\lambda_X = 550$ nm is fixed, while the other (λ_Y) is varied from 450 nm to 650 nm in steps of 10 nm. Each simulation consists of an initial population of 20 random individuals, which is evolved for 200 generations. At the end of the evolution, the structure with the most similar $Q_{\text{scat}}(\lambda_X)$ and $Q_{\text{scat}}(\lambda_Y)$ is chosen from each simulation (like structure (2) in Fig. 4).

In Figure 5, we show the resulting structures (a) and their GDM-simulated spectra for X - and Y -polarized incidence (b). The different λ_Y are indicated by a color coding from blue ($\lambda_Y = 450$ nm) to red ($\lambda_Y = 650$ nm). As explained in the previous subsection, for increasing wavelengths, the four sub-antennas tend to combine in only two structures (instead of more constituents for the shortest wavelengths), which is due to the limited amount of allowed material. For the same reason, at wavelengths above 600 nm all sub-antennas are even merged into one single structure, and for the longest wavelengths the available material is not sufficient to yield a satisfactory maximization (for an analysis of the role of the constrained amount of material, see [SI, Secs. E and F](#)).

For an experimental verification, we fabricated Si-structures corresponding to the optimized color-tuned

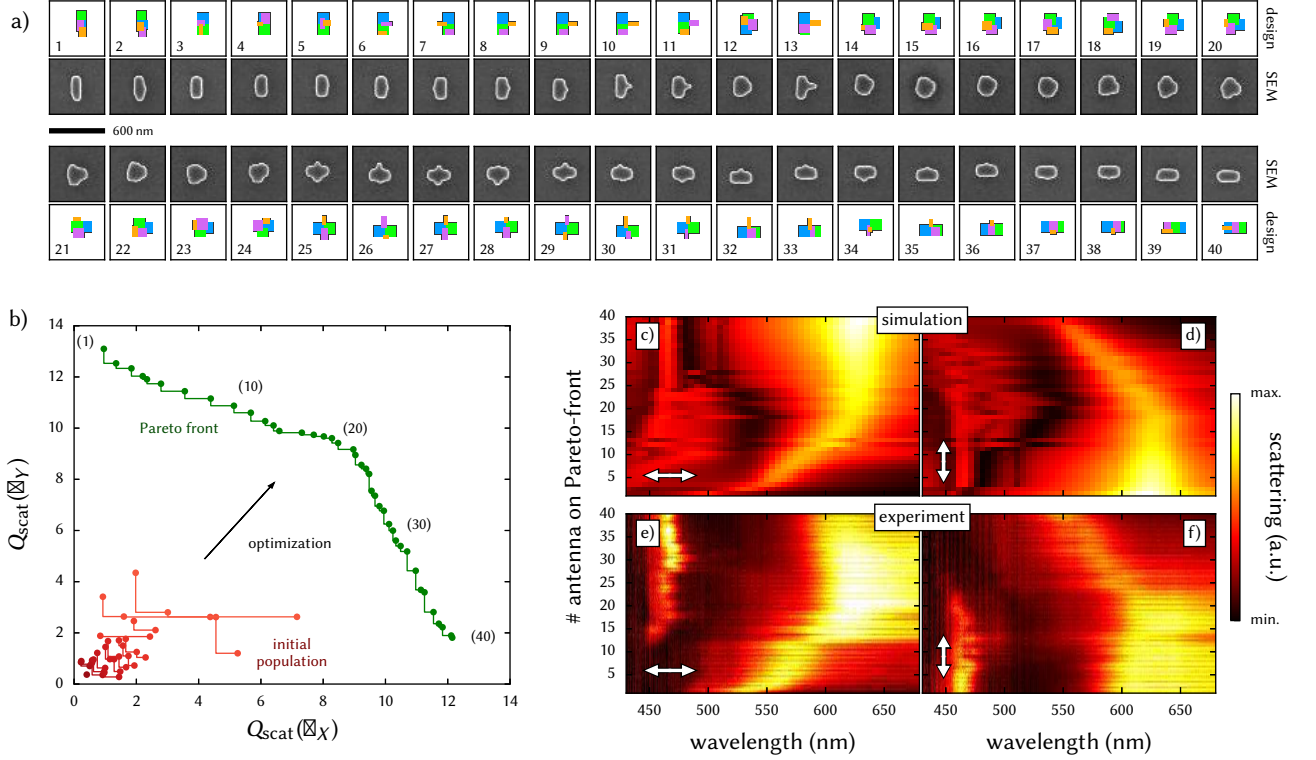


FIG. 3. **Results of EMO-GDM for identical target wavelengths $\lambda_X = \lambda_Y = 630$ nm.** (a) Structures of the Pareto-front and corresponding SEM images. All fields are 600×600 nm² large. Blue, green, purple and orange dots are used to highlight the positions of the sub-blocks the structures consist of. (b) Pareto-front (green) and randomized initial population (red). (c-f) Scattering spectra for X (left) and Y polarization (right). Simulated and experimental spectra are shown in the top and bottom rows, respectively.

nanoantennas. SEM images (Fig. 5c) and polarization filtered dark-field spectra (Fig. 5d, top: filter along X, bottom: along Y) are shown in figure 5. Polarization filtered dark-field images (Fig. 1d and insets in Fig. 5d) of color-switching pictograms, composed of the optimized structures, demonstrate the polarization dependence of the scattered wavelengths.

By a closer look on the individual structures, we observe that the “symmetric” optimization with $\lambda_X = \lambda_Y = 550$ nm results in a non-symmetric particle. We would intuitively expect a point-symmetric antenna (*i.e.* of S_2 symmetry group) to be ideally suited for equally strong scattering under both, X- and Y-polarization. The evolutionary optimization, being a non-analytic routine, should at least result in some “quasi”-symmetric structures, which is however not the case here. As before, this can be explained by the finite amount of material available in our structure model. Because the T-shaped part of the antenna already consists of three of the four sub-antennas, the fourth sub-antenna is added as a square block of maximum allowed dimension, and it is impossible for the algorithm to generate a symmetric structure within the given constraints. As shown in the supporting informations, a simulation with $\lambda_X = \lambda_Y = 450$ nm as well as an optimization with relaxed constraints on

the antenna size results in quasi-symmetric structures, as intuitively expected (see SI, Sec. G).

Again, for $\lambda_X = \lambda_Y = 550$ nm, interference between both parts of the antenna results in an optimum scattering efficiency at the target wavelength and therefore exact positioning of the constituents is crucial: A change of the spacing between the T-shaped and squared sub-structures by $\Delta x = 100$ nm already results in a decrease of more than 5 % in scattering efficiency for at least one polarization. An analysis of the $\lambda_X = \lambda_Y = 550$ nm antenna can be found in the supporting informations (Sec. D, Fig. S6).

In summary, we emphasize that despite the simplicity of the designs generated by the EMO, all the parameters (sizes, positions, distances) were nearly perfectly optimized by the evolutionary algorithm. We conclude that the EMO-GDM technique is able to find ideal nanostructures even within narrow constraints on parameters like the size, the available amount of material or discrete step-sizes for compatibility with nanofabrication technology.

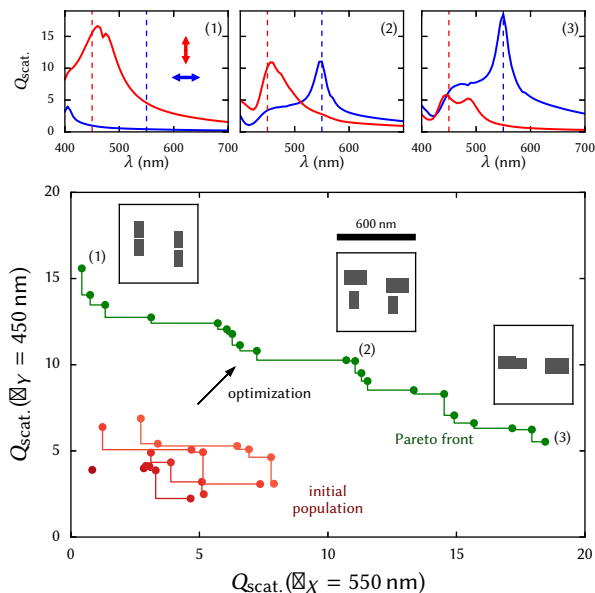


FIG. 4. **Pareto-front example of an optimization run with $\lambda_X = 550$ nm and $\lambda_Y = 450$ nm.** Top: Spectra of selected antennas (indicated by numbers on Pareto front), where either a single wavelength is optimized (1 and 3) or both resonance wavelengths are scattered approximately equally (2). X (Y) polarized illumination is plotted with blue (red) color. The selected structures are sketched in the insets, showing areas of 600×600 nm².

D. Polarization Encoded Micro Images

To illustrate the previous results we produced small images, only few micrometers large, composed of EMO-optimized antennas. The absolute scattering cross section σ_{scat} was used as the optimization target. An additional spacing of 250 nm is used between the individual particles, which results in pixel sizes of 850×850 nm² (≈ 30000 dpi), close to the diffraction limit.

Polarization-filtered dark field images are shown in figure 6. Depending on the orientation of the polarization filter (left: X , right: Y), one single arrow is visible, pointing in the corresponding direction while the second arrow vanishes in a blue background. Furthermore, the logos of the CNRS and CEMES laboratory are nested into one image, encoded in perpendicular polarizations. A scheme of the lithographic mask (red) and a SEM image (grey) of a zoom into the logos, indicated by small yellow squares, is shown at the bottom. We attribute the slightly reminiscent signatures of the hidden motifs to intensity-variations due to the arrangement of the antennas in grating-like 2D-arrays (see also SI Sec. H).

III. CONCLUSIONS

In conclusion, we presented a technique of evolutionary multi-objective optimization coupled to full-field electro-

dynamical simulations for the automatic design of photonic nanostructures. We successfully demonstrated the method on the design of polarization-dependent dual-resonant silicon scatterers in the visible spectral range. Such silicon nanostructures are of great interest as alternatives to plasmonic particles. However due to their multi-modal optical behavior it is often difficult to find appropriate geometries. We demonstrated that our EMO approach is able to design double-resonant dielectric nanoantennas even within a very simple and strongly constrained structure-model. For a maximum compatibility with fabrication methods, technological limitations were included as boundary conditions in the model. Due to these technological considerations, we were able to produce samples on SOI substrate using the outcome of the optimizations for a lithographic mask. With polarization filtered dark-field microscopy we finally confirmed the agreement between samples and simulations.

A great advantage of the EMO-GDM technique is its flexibility and the ability to self-adapt to arbitrary limitations. Additional constraints can easily be implemented because no analytical treatment of the input model needs to be performed. Inadequate structures, inconsistent with the constraint functions, are being discarded automatically during the evolution and only technologically convenient designs are generated. The method can also be easily extended for the rigorous design of metasurfaces, where interference between the unit cells needs to be considered. Periodic boundary conditions can be included in the GDM by means of an appropriate Green's Dyad.^{42,43} In this way, the distance between substructures on the metasurface may also be included as a free parameter in the optimization. We believe that multi-objective optimization of photonic nanostructures has a tremendous potential for many kinds of possible applications in near- and far-field nano-optics for example in the design of multiresonant, broadband light harvesting, or nonlinear nanostructures.

IV. METHODS

A. EMO-GDM method

We use the python interface of the parallel evolutionary multi-objective optimization (EMO) toolkit paGMO/pyGMO⁴⁴ and in particular its implementation of the “SMS-EMOA” algorithm⁴⁵. A comprehensive introduction to evolutionary multi-objective optimization can be found in reference 32.

All interfacing between the EMO and the electro-dynamical full-field solver is implemented in python. The fitness of each nanoparticle is calculated using the Green Dyadic Method (GDM), which is implemented in fortran to yield high computational speed.

The target nanoparticle is discretized in N cubic mesh-points of side-length b , for each of which a dipolar response is assumed. This approach eventually leads to

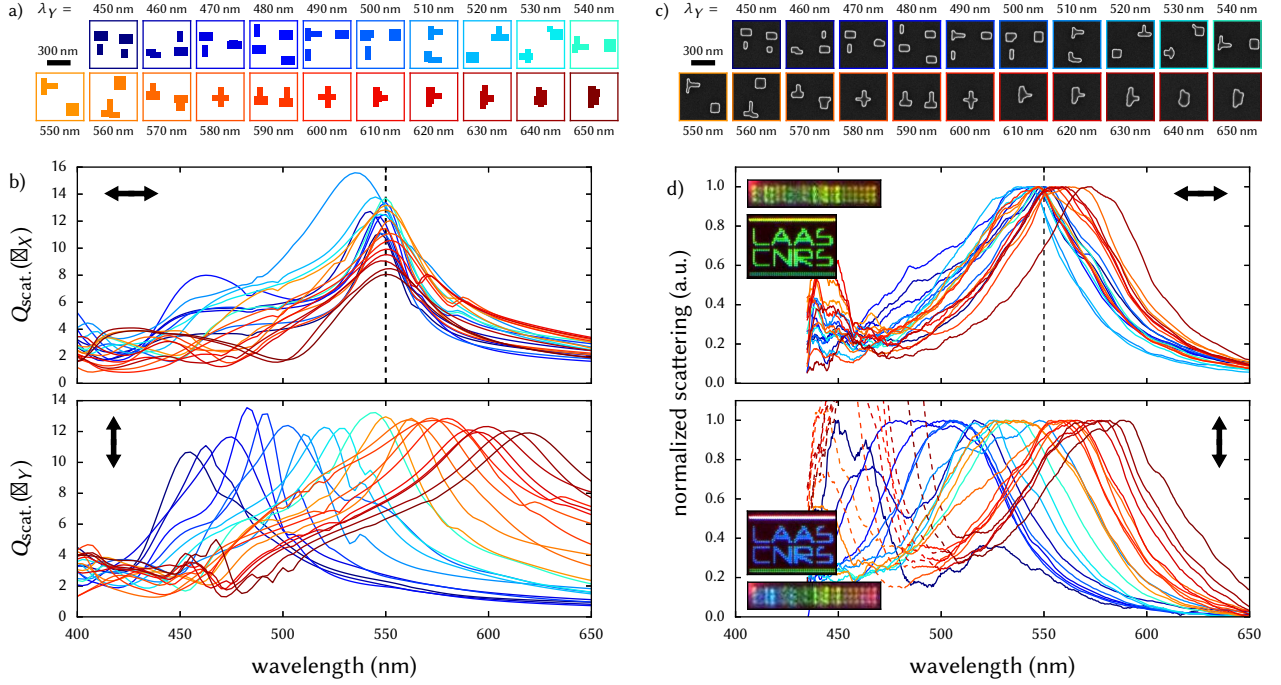


FIG. 5. **Experimental demonstration of several dual-resonant Si structures based on EMO-GDM simulations.** (a) EMO design of multi-resonant dielectric particles and (b) simulated scattering spectra for $\lambda_X = 550$ nm (indicated by a black dashed line) and various λ_Y . (c) SEM images and (d) polarization filtered scattering spectra of the corresponding nanofabricated sample. Insets in (d) show polarization filtered dark-field microscopy images of the full set of structures ($20 \times 4 \mu\text{m}^2$) and of the LAAS laboratory logo ($35 \times 23 \mu\text{m}^2$). The lines framing the blue letters ($\lambda_Y = 450$ nm) are optimized for $\lambda_Y = 650$ nm (upper line) and $\lambda_Y = 570$ nm (lower line). Areas in a) and c) are $600 \times 600 \text{ nm}^2$.

a system of $3N$ coupled equations that relates an incident electric field \mathbf{E}_0 to the field \mathbf{E} due to the particle's response:

$$\mathbf{E}_0 = \mathbf{M} \cdot \mathbf{E}. \quad (1)$$

The field in the structure can then be obtained by an inversion of the matrix \mathbf{M} , which is composed of 3×3 sub-matrices

$$\mathbf{M}_{ij} = \mathbf{I} \cdot \delta_{ij} - \alpha_i(\omega) \mathbf{G}(\mathbf{r}_i, \mathbf{r}_j, \omega). \quad (2)$$

Here, \mathbf{I} is the Cartesian unitary tensor, δ_{ij} the Kronecker delta function and (cgs units)

$$\alpha_i(\omega) = \frac{\epsilon_i(\omega) - \epsilon_{\text{env.}}(\omega)}{4\pi} \cdot v_i. \quad (3)$$

v_i is the volume of each cubic cell, in our case $v_i = b^3$. For the permittivity ϵ_i we use the dispersion of silicon from Ref. 46 and assume a constant environment of $\epsilon_{\text{env.}} = 1$.

\mathbf{G} is the Green's Dyad which couples the dipolar elements i and j and is composed of a vacuum and a surface term

$$\mathbf{G}(\mathbf{r}_i, \mathbf{r}_j, \omega) = \mathbf{G}_0(\mathbf{r}_i, \mathbf{r}_j, \omega) + \mathbf{G}_{\text{surf}}(\mathbf{r}_i, \mathbf{r}_j, \omega) \quad (4)$$

which can be found in literature.⁴⁷ To account for the divergence of the Green's function at $\mathbf{r}_i = \mathbf{r}_j$, a normalization scheme

$$\mathbf{G}_0(\mathbf{r}_i, \mathbf{r}_i, \omega) = \mathbf{I}C(\omega) \quad (5)$$

is introduced, which writes for a cubic mesh

$$C(\omega) = -\frac{4\pi}{3} \frac{1}{\epsilon_{\text{env.}}(\omega)v_i} \quad (6)$$

and has to be adapted together with the cell volume, if a different meshing is used like, for example a hexagonal compact grid.⁴⁷

Finally, the matrix inversion is done using standard LU-decomposition and the scattering efficiencies can be calculated from the nearfield \mathbf{E} inside the particle.⁴⁸

A great advantage of the GDM is that the presence of a substrate (in our case $n = 1.5$) can be taken into account by means of an appropriate Green's Dyadic function (Eq. (4)), thus at almost no supplementary computational cost. In comparison to finite-difference time-domain (FDTD) simulations, a frequency-domain method has further advantages with regards to our purpose of designing a doubly resonant nanostructure: So-called perfectly matched layers are not needed and only the nanoparticle itself is subject to the volume discretization. Generally, this results in a quicker convergence.

The amount of silicon per antenna is not constant in our model and as the duration of a simulation is depending on the structure size, the optimizations generally tend to be slower for longer resonance wavelengths, because of resulting larger particles. Nevertheless, evolutions of populations with 20 individuals over 200 generations take

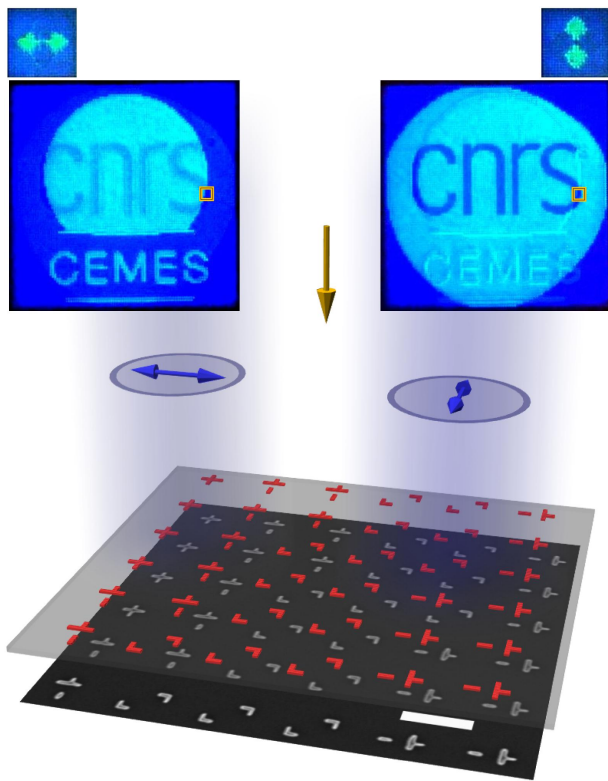


FIG. 6. **Polarization-filtered dark-field images of micrometer scale EMO-based pictures.** Micrometer scale pictures composed of 24×24 (arrows) and 100×100 (logos) EMO-GDM designed particles. A linear polarization filter is added before the camera, oriented along X (top, left) and along Y (top, right). Arrow images are $15 \times 15 \mu\text{m}^2$, logos $60 \times 60 \mu\text{m}^2$ large. Bottom image: Zoom into the logo-picture. SEM image in grey (scalebar is 500 nm) and sketch of the lithographic mask in red, highlighted by small yellow squares in the dark-field images. The yellow arrow and blue emission indicate the incident and scattered light, respectively.

not longer than around 10-15 hours on one single core of a 2.8 GHz Intel Xeon E5-1603 CPU. We note that the results were always reproducible, yielding very similar structures and scattering efficiencies from multiple runs

B. E-Beam Lithography on SOI

Samples were fabricated in a top-down approach that couples Electron Beam Lithography (EBL) with anisotropic plasma etching. This was used to pattern the designed nanostructures^{49,50} on a silicon-on-insulator (SOI) wafer as substrate (Si: 95 nm, BOX: 145 nm). The EBL was carried out with a RAITH 150 writer at an energy of 30 keV on a thin (60nm) negative-tone resist layer, namely hydrogen silsesquioxane (HSQ). After exposure,

HSQ was developed by immersion in 25 % tetramethylammonium hydroxide (TMAH) for 1 min. HSQ patterns were subsequently transferred to the silicon top layer by reactive ion etching in a SF₆/C₄F₈ plasma based chemistry down to the buried oxide layer.

In the EMO runs, the minimum feature size was set to 60 nm to avoid removing small features of the structures during lift-off. The structures were discretized and placed on a grid by steps of 20 nm to match the precision of the EBL. SEM images of individual structures are shown and are compared to the mask-layout in Figs. 3, 5 and 6.

C. Confocal Dark-Field Microscopy

Confocal optical dark-field microscopy was performed on a conventional spectrometer (Horiba XploRA). A spectrally broad white lamp was focused on the sample by a $\times 50$, NA 0.45 dark-field objective, backscattered, polarization filtered and dispersed by a 300 grooves per mm grating onto an Andor iDus 401 CCD. The intensity distribution of the lamp as well as the spectral response of the optical components was accounted for by subtracting the background measured on bare SOI and normalizing the measured spectra to a white reference sample.

ACKNOWLEDGMENTS

The authors thank P. Salles and G.-M. Caruso for technical assistance. This work was partly supported under “Campus Gaston Dupouy” grant by French government, Région Midi-Pyrénées and European Union (ERDF), by the computing facility center CALMIP of the University of Toulouse under grant P12167 and by LAAS-CNRS micro and nanotechnologies platform member of the French RENATECH network.

V. AUTHOR CONTRIBUTIONS

P.W., V.P. and A.A. designed the research. C.G., A.A. and P.W. implemented the codes and performed the simulations. A.L. and G.L. fabricated the samples by EBL. P.W. and V.P. performed the dark-field scattering experiments. All authors contributed to the data analysis, figure preparation and manuscript writing.

VI. SUPPORTING INFORMATION

Details and considerations on the optimization method and on the GDM, further simulations, detailed analysis of several EMO-designed antennas and a discussion on grating-like effects from the arrangement of structures in 2D-arrays (PDF).

- ¹ Tan, S. J. *et al.* Plasmonic Color Palettes for Photorealistic Printing with Aluminum Nanostructures. *Nano Letters* **14**, 4023–4029 (2014). URL <http://dx.doi.org/10.1021/nl501460x>.
- ² Lindfors, K. *et al.* Imaging and Steering Unidirectional Emission from Nanoantenna Array Metasurfaces. *ACS Photonics* **3**, 286–292 (2016). URL <http://dx.doi.org/10.1021/acsphotonics.5b00646>.
- ³ Black, L.-J., Wang, Y., de Groot, C. H., Arbouet, A. & Muskens, O. L. Optimal Polarization Conversion in Coupled Dimer Plasmonic Nanoantennas for Metasurfaces. *ACS Nano* **8**, 6390–6399 (2014). URL <http://dx.doi.org/10.1021/nn501889s>.
- ⁴ Baffou, G., Quidant, R. & Girard, C. Heat generation in plasmonic nanostructures: Influence of morphology. *Applied Physics Letters* **94**, 153109 (2009). URL <http://scitation.aip.org/content/aip/journal/apl/94/15/10.1063/1.3116645>.
- ⁵ Valev, V. K., Baumberg, J. J., Sibilia, C. & Verbiest, T. Chirality and Chiroptical Effects in Plasmonic Nanostructures: Fundamentals, Recent Progress, and Outlook. *Advanced Materials* **25**, 2517–2534 (2013). URL <http://onlinelibrary.wiley.com/doi/10.1002/adma.201205178/abstract>.
- ⁶ Kauranen, M. & Zayats, A. V. Nonlinear plasmonics. *Nature Photonics* **6**, 737–748 (2012). URL <http://www.nature.com/nphoton/journal/v6/n11/full/nphoton.2012.244.html>.
- ⁷ Albella, P., Alcaraz de la Osa, R., Moreno, F. & Maier, S. A. Electric and Magnetic Field Enhancement with Ultralow Heat Radiation Dielectric Nanoantennas: Considerations for Surface-Enhanced Spectroscopies. *ACS Photonics* **1**, 524–529 (2014). URL <http://dx.doi.org/10.1021/ph500060s>.
- ⁸ Bakker, R. M. *et al.* Magnetic and Electric Hotspots with Silicon Nanodimers. *Nano Letters* **15**, 2137–2142 (2015). URL <http://dx.doi.org/10.1021/acs.nanolett.5b00128>.
- ⁹ Ginn, J. C. *et al.* Realizing Optical Magnetism from Dielectric Metamaterials. *Physical Review Letters* **108**, 097402 (2012). URL <http://link.aps.org/doi/10.1103/PhysRevLett.108.097402>.
- ¹⁰ Kuznetsov, A. I., Miroshnichenko, A. E., Fu, Y. H., Zhang, J. & Luk'yanchuk, B. Magnetic light. *Scientific Reports* **2**, 492 (2012). URL <http://www.nature.com/articles/srep00492>.
- ¹¹ Albella, P. *et al.* Low-Loss Electric and Magnetic Field-Enhanced Spectroscopy with Subwavelength Silicon Dimers. *The Journal of Physical Chemistry C* **117**, 13573–13584 (2013). URL <http://dx.doi.org/10.1021/jp4027018>.
- ¹² Yu, Y. F. *et al.* High-transmission dielectric metasurface with 2π phase control at visible wavelengths. *Laser & Photonics Reviews* **9**, 412–418 (2015). URL <http://onlinelibrary.wiley.com/doi/10.1002/lpor.201500041/abstract>.
- ¹³ Shcherbakov, M. R. *et al.* Enhanced Third-Harmonic Generation in Silicon Nanoparticles Driven by Magnetic Response. *Nano Letters* **14**, 6488–6492 (2014). URL <http://dx.doi.org/10.1021/nl503029j>.
- ¹⁴ Wiecha, P. R. *et al.* Enhanced nonlinear optical response from individual silicon nanowires. *Physical Review B* **91**, 121416 (2015). URL <http://link.aps.org/doi/10.1103/PhysRevB.91.121416>.
- ¹⁵ Fu, Y. H., Kuznetsov, A. I., Miroshnichenko, A. E., Yu, Y. F. & Luk'yanchuk, B. Directional visible light scattering by silicon nanoparticles. *Nature Communications* **4**, 1527 (2013). URL <http://www.nature.com/ncomms/journal/v4/n2/full/ncomms2538.html>.
- ¹⁶ Schmidt, M. K. *et al.* Dielectric antennas - a suitable platform for controlling magnetic dipolar emission. *Optics Express* **20**, 13636 (2012). URL <https://www.osapublishing.org/oe/abstract.cfm?uri=oe-20-13-13636>.
- ¹⁷ Cao, L., Fan, P., Barnard, E. S., Brown, A. M. & Brongersma, M. L. Tuning the Color of Silicon Nanostructures. *Nano Letters* **10**, 2649–2654 (2010). URL <http://dx.doi.org/10.1021/nl1013794>.
- ¹⁸ Traviss, D. J., Schmidt, M. K., Aizpurua, J. & Muskens, O. L. Antenna resonances in low aspect ratio semiconductor nanowires. *Optics Express* **23**, 22771 (2015). URL <https://www.osapublishing.org/abstract.cfm?URI=oe-23-17-22771>.
- ¹⁹ Zhao, W. *et al.* Full-color hologram using spatial multiplexing of dielectric metasurface. *Optics Letters* **41**, 147 (2016). URL <https://www.osapublishing.org/abstract.cfm?URI=ol-41-1-147>.
- ²⁰ Sivanandam, S. & Deepa, S. *Introduction to Genetic Algorithms* (Springer, Heidelberg, 2008). URL <http://link.springer.com/book/10.1007/978-3-540-73190-0>.
- ²¹ Forestiere, C. *et al.* Particle-swarm optimization of broadband nanoplasmonic arrays. *Optics Letters* **35**, 133 (2010). URL <https://www.osapublishing.org/ol/abstract.cfm?uri=ol-35-2-133>.
- ²² Feichtner, T., Selig, O., Kiunke, M. & Hecht, B. Evolutionary Optimization of Optical Antennas. *Physical Review Letters* **109**, 127701 (2012). URL <http://link.aps.org/doi/10.1103/PhysRevLett.109.127701>.
- ²³ Forestiere, C. *et al.* Genetically Engineered Plasmonic Nanoarrays. *Nano Letters* **12**, 2037–2044 (2012). URL <http://dx.doi.org/10.1021/nl300140g>.
- ²⁴ Forestiere, C., He, Y., Wang, R., Kirby, R. M. & Dal Negro, L. Inverse Design of Metal Nanoparticles' Morphology. *ACS Photonics* **3**, 68–78 (2016). URL <http://dx.doi.org/10.1021/acsphotonics.5b00463>.
- ²⁵ Ginzburg, P., Berkovitch, N., Nevet, A., Shor, I. & Orenstein, M. Resonances On-Demand for Plasmonic Nanoparticles. *Nano Letters* **11**, 2329–2333 (2011). URL <http://dx.doi.org/10.1021/nl200612f>.
- ²⁶ Macías, D., Adam, P.-M., Ruíz-Cortés, V., Rodríguez-Oliveros, R. & Sánchez-Gil, J. A. Heuristic optimization for the design of plasmonic nanowires with specific resonant and scattering properties. *Optics Express* **20**, 13146 (2012). URL <https://www.osapublishing.org/oe/abstract.cfm?uri=oe-20-12-13146>.
- ²⁷ Bigourdan, F., Marquier, F., Hugonin, J.-P. & Greffet, J.-J. Design of highly efficient metallo-dielectric patch antennas for single-photon emission. *Optics Express* **22**, 2337 (2014). URL <https://www.osapublishing.org/oe/abstract.cfm?uri=oe-22-3-2337>.

- ²⁸ Chen, P. Y., Chen, C. H., Wu, J. S., Wen, H. C. & Wang, W. P. Optimal design of integrally gated CNT field-emission devices using a genetic algorithm. *Nanotechnology* **18**, 395203 (2007). URL <http://stacks.iop.org/0957-4484/18/i=39/a=395203?key=crossref.d374430889ccb7bbffbf78b97103aeb0>.
- ²⁹ Mengyu Wang, Aytac Alparslan, Sascha M. Schnepf & Christian Hafner. Optimization of a Plasmon-Assisted Waveguide Coupler Using FEM and MMP. *Progress In Electromagnetics Research B* **59**, 219–229 (2014).
- ³⁰ Kessentini, S., Barchiesi, D., Grosjes, T. & Lamy de la Chapelle, M. Particle swarm optimization and evolutionary methods for plasmonic biomedical applications. In *2011 IEEE Congress on Evolutionary Computation (CEC)*, 2315–2320 (2011).
- ³¹ Jung, J. Robust Design of Plasmonic Waveguide Using Gradient Index and Multiobjective Optimization. *IEEE Photonics Technology Letters* **28**, 756–758 (2016).
- ³² Deb, K. *Multi-objective optimization using evolutionary algorithms*, vol. 16 (Wiley, 2001).
- ³³ Shegai, T. *et al.* A bimetallic nanoantenna for directional colour routing. *Nature Communications* **2**, 481 (2011). URL <http://www.nature.com/ncomms/journal/v2/n9/full/ncomms1490.html>.
- ³⁴ Aouani, H. *et al.* Ultrasensitive Broadband Probing of Molecular Vibrational Modes with Multifrequency Optical Antennas. *ACS Nano* **7**, 669–675 (2013). URL <http://dx.doi.org/10.1021/nn304860t>.
- ³⁵ Dopf, K. *et al.* Coupled T-Shaped Optical Antennas with Two Resonances Localized in a Common Nanogap. *ACS Photonics* **2**, 1644–1651 (2015). URL <http://dx.doi.org/10.1021/acsp Photonics.5b00446>.
- ³⁶ Harutyunyan, H., Volpe, G., Quidant, R. & Novotny, L. Enhancing the Nonlinear Optical Response Using Multifrequency Gold-Nanowire Antennas. *Physical Review Letters* **108**, 217403 (2012). URL <http://link.aps.org/doi/10.1103/PhysRevLett.108.217403>.
- ³⁷ Celebrano, M. *et al.* Mode matching in multiresonant plasmonic nanoantennas for enhanced second harmonic generation. *Nature Nanotechnology* **10**, 412–417 (2015). URL <http://www.nature.com/nnano/journal/v10/n5/full/nnano.2015.69.html>.
- ³⁸ Girard, C. Near fields in nanostructures. *Reports on Progress in Physics* **68**, 1883–1933 (2005). URL <http://stacks.iop.org/0034-4885/68/i=8/a=R05?key=crossref.0a49722c35b5f8f658773d36f47aa4be>.
- ³⁹ Goh, X. M., Ng, R. J. H., Wang, S., Tan, S. J. & Yang, J. K. Comparative Study of Plasmonic Colors from All-Metal Structures of Posts and Pits. *ACS Photonics* **Article ASAP** (2016). URL <http://dx.doi.org/10.1021/acsp Photonics.6b00099>.
- ⁴⁰ Li, Z., Clark, A. W. & Cooper, J. M. Dual Color Plasmonic Pixels Create a Polarization Controlled Nano Color Palette. *ACS Nano* **10**, 492–498 (2016). URL <http://dx.doi.org/10.1021/acsnano.5b05411>.
- ⁴¹ Martin, O. J. F., Girard, C. & Dereux, A. Generalized Field Propagator for Electromagnetic Scattering and Light Confinement. *Physical Review Letters* **74**, 526–529 (1995). URL <http://link.aps.org/doi/10.1103/PhysRevLett.74.526>.
- ⁴² Chaumet, P. C. & Sentenac, A. Simulation of light scattering by multilayer cross-gratings with the coupled dipole method. *Journal of Quantitative Spectroscopy and Radiative Transfer* **110**, 409–414 (2009). URL <http://www.sciencedirect.com/science/article/pii/S0022407308002707>.
- ⁴³ Gallinet, B. & Martin, O. J. F. Electromagnetic Scattering of Finite and Infinite 3d Lattices in Polarizable Backgrounds. *Theoretical And Computational Nanophotonics (Tacona-Photonics 2009)* **1176**, 63–65 (2009). URL <http://infoscience.epfl.ch/record/164792>.
- ⁴⁴ Biscani, F., Izzo, D. & Yam, C. H. A Global Optimisation Toolbox for Massively Parallel Engineering Optimisation. *arXiv:1004.3824 [cs, math]* (2010). URL <http://arxiv.org/abs/1004.3824>. ArXiv: 1004.3824.
- ⁴⁵ Beume, N., Naujoks, B. & Emmerich, M. SMS-EMOA: Multiobjective selection based on dominated hypervolume. *European Journal of Operational Research* **181**, 1653–1669 (2007). URL <http://www.sciencedirect.com/science/article/pii/S0377221706005443>.
- ⁴⁶ Edwards, D. F. Silicon (Si)*. In Palik, E. D. (ed.) *Handbook of Optical Constants of Solids*, 547 – 569 (Academic Press, Burlington, 1997). URL <http://www.sciencedirect.com/science/article/pii/B9780125444156500273>.
- ⁴⁷ Girard, C., Dujardin, E., Baffou, G. & Quidant, R. Shaping and manipulation of light fields with bottom-up plasmonic structures. *New Journal of Physics* **10**, 105016 (2008). URL <http://iopsience.iop.org/1367-2630/10/10/105016>.
- ⁴⁸ Draine, B. T. The Discrete-Dipole Approximation and its Application to Interstellar Graphite Grains. *Astrophysical Journal* **333**, 848–872 (1988).
- ⁴⁹ Han, X.-L., Larrieu, G., Fazzini, P.-F. & Dubois, E. Realization of ultra dense arrays of vertical silicon nanowires with defect free surface and perfect anisotropy using a top-down approach. *Microelectronic Engineering* **88**, 2622–2624 (2011). URL <http://www.sciencedirect.com/science/article/pii/S0167931710005903>.
- ⁵⁰ Guerfi, Y., Carcenac, F. & Larrieu, G. High resolution HSQ nanopillar arrays with low energy electron beam lithography. *Microelectronic Engineering* **110**, 173–176 (2013). URL <http://www.sciencedirect.com/science/article/pii/S0167931713002724>.